Remaining discharge energy prediction for lithium-ion batteries over broad current ranges: A machine learning approach

Hao Tu [a], Manashita Borah [b,c], Scott Moura [c], Yebin Wang [d], Huazhen Fang [a,*]

[a] *Department of Mechanical Engineering, University of Kansas, Lawrence, KS 66045, USA*
[b] *Department of Electrical Engineering, Tezpur University, Tezpur, 784028, India*
[c] *Department of Civil and Environmental Engineering, University of California, Berkeley, CA 94720, USA*
[d] *Mitsubishi Electric Research Laboratories, Cambridge, MA 02139, USA*

ARTICLE INFO

ABSTRACT

Lithium-ion batteries have found their way into myriad sectors of industry to drive electrification, decarbonization, and sustainability. A crucial aspect in ensuring their safe and optimal performance is monitoring their energy levels. In this paper, we present the first study on predicting the remaining energy of a battery cell undergoing discharge over wide current ranges from low to high C-rates. The complexity of the challenge arises from the cell's C-rate-dependent energy availability as well as its intricate electro-thermal dynamics especially at high C-rates. To address this, we introduce a new definition of remaining discharge energy and then undertake a systematic effort in harnessing the power of machine learning to enable its prediction. Our effort includes two parts in cascade. First, we develop an accurate dynamic model based on integration of physics with machine learning to capture a battery's voltage and temperature behaviors. Second, based on the model, we propose a machine learning approach to predict the remaining discharge energy under arbitrary C-rates and pre-specified cut-off limits in voltage and temperature. The experimental validation shows that the proposed approach can predict the remaining discharge energy with a relative error of less than 3% when the current varies between 0~8 C for an NCA cell and 0~15 C for an LFP cell. The approach, by design, is amenable to training and computation.

1. Introduction

Lithium-ion batteries (LiBs) represent one of the most important power source technologies of our time. They have transformed the consumer electronics sector since the 1990s and are now driving the revolution of transportation electrification that extends from passenger cars to commercial vehicles to aircraft. Battery management systems (BMSs) must be in place to ensure LiBs' operational safety and performance. Among the various BMS functions, a significant one is monitoring the state of energy or, more specifically, the remaining discharge energy (RDE). While its definition may take different forms, the RDE generally indicates how much energy is available before the cell gets depleted in discharging. Practical applications demand accurate, real-time RDE prediction to avoid over-discharging or to determine the remaining duration or range in power supply. However, the prediction is non-trivial due to the complex dynamics of LiBs, which has attracted a growing body of research in recent years.

Closely related to the RDE, a more familiar quantity in the literature is the so-called state-of-charge (SoC), which is the percentage ratio between a cell's available charge capacity in ampere-hours (Ah) and its nominal capacity. While the estimation of it has received extensive study [1–8], the SoC does not align with the cell's actual level of energy in watt-hours (Wh) [9]. As a case in point, the amount of energy the cell can deliver in the low SoC range is less than that in the high SoC range. By definition, the SoC also factors out the rate-capacity effect, which refers to the phenomenon of the deliverable charge or energy capacity becoming less (resp. more) under higher (resp. lower) discharging C-rates [10].

Compared to the SoC, the RDE comes as a more direct measure of the cell's remaining energy. RDE prediction has attracted growing interest, and the studies to date fall into two categories. The first category regards RDE as a synonym of SoC, naming it as state-of-energy (SoE). Firstly proposed in [9], SoE is defined as the percentage ratio of the cell's present energy capacity in Wh over the maximum energy capacity in Wh [9]. The challenge in SoE estimation mainly lies in SoE modeling. One way is to relate the SoE with OCV [11] and SoC [12–14] and then compute it based on these quantities. Another way is to build

---

dynamic SoE models supplemented with the measurements of current, voltage, and temperature [15]. Given these models, one can apply various state estimation methods, such as Kalman filtering [16,17] and particle filtering [18,19], to estimate SoE. However, SoE estimation has not accounted for the effects of different discharging conditions, e.g., C-rates and temperature, on the actual energy availability [15].

The second category considers a literal definition of RDE — the integral of future discharging (the product of current and voltage) over time. This approach runs the cell's dynamic model forward under a specific future current load until certain cut-off limits are reached and then performs numerical integration to determine the RDE. Some studies pursue the prediction of future current profiles by weighted moving average [20] and Markov modeling [21,22], and subsequently incorporate these predictions into the RDE calculation. However, the methods in this category generally focus on discharging at low to medium C-rates. As another limitation, the model forward simulation requires substantial amounts of computation, even though equivalent circuit models (ECMs) are commonly used.

Despite the many promising developments in RDE prediction, the state of the art is still limited. Existing works generally consider discharging at low to medium currents. In this case, the RDE is almost linear with the SoC [10], so the estimation of RDE bears little difference from SoC estimation. However, more interesting and useful is RDE prediction for discharging that spans low to high currents. This problem conveys more challenges while proving crucial for some emerging applications like electric aircraft [23], but the literature is void of studies to deal with it. We also note that some RDE prediction methods, e.g., those based on model-based forward simulation, require heavy computation. Practical applications, however, demand methods that are computationally efficient and amenable to implementation.

Motivated to overcome the above limitations, this paper, for the first time, explores the intricate task of RDE prediction over broad C-rate ranges and develops a solution framework based on machine learning (ML). The contribution is threefold.

- We propose a new RDE definition aligned with the considered problem. Different from its counterparts in the literature, the definition makes RDE dependent on C-rates and accounts for the effects of both the voltage limit and temperature limit.
- Following the definition, we develop an ML approach to make RDE prediction. The proposed ML architecture combines different learning modules, which are tasked to predict first the remaining time for discharging and then the remaining energy under specified C-rates and temperature and voltage limits. We provide the technical rationale to justify the design of each learning module.
- We propose to train the proposed ML approach on synthetic data, as otherwise the training would need a large number of discharging tests. To obtain high-fidelity synthetic data, we develop a separate hybrid physics+ML model capable of delivering accurate voltage and temperature prediction over broad current ranges. This hybrid model is an extension of our prior work in [24], which is trained on experimental datasets.

The proposed RDE prediction approach is accurate, tractable for training, and computationally fast. We validate its effectiveness through extensive experiments on a nickel–cobalt–aluminum (NCA) cell and a lithium–iron–phosphate (LFP) cell.

Tangentially related with our work is using ML for other battery management tasks, such as SoC estimation, remaining useful life prediction, and fault detection. An interested reader is referred to [25–28] and the references therein. Our work in this paper, however, is distinct from the literature in two ways. First, we consider the new problem of RDE prediction when the current ranges from low to high C-rates, the complexity of which makes ML especially useful. Second, we present a unique, customized ML design for the considered problem.

The remainder of the paper is organized as follows. Section 2 proposes the definition of the C-rate-dependent RDE. Section 3 presents the
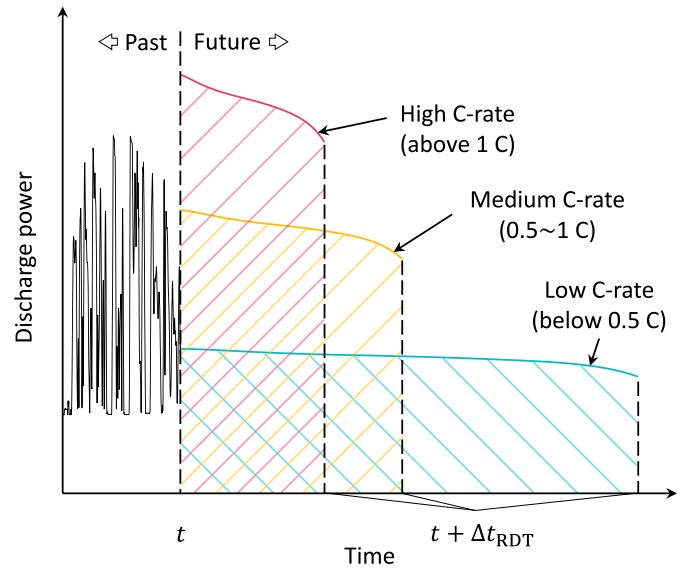

Fig. 1. Illustration of the proposed C-rate-dependent RDE definition for LiBs. The shaded areas represent the RDE at different discharging C-rate levels. The present time is t and the remaining discharge time is Δt_{RDT}.

hybrid physics-ML model to predict a LiB cell's voltage and temperature in discharging over broad current ranges. Section 4 presents an ML-based RDE prediction approach. Then, the experimental validation results are shown in Section 5. Finally, Section 6 concludes the paper.

2. Definition of C-rate-dependent RDE

This section proposes a new definition of RDE for LiBs. Different from other versions, this definition is designed to capture the variation of a cell's remaining available energy over different C-rates. Accurate and real-time prediction of the proposed RDE will be the aim of the subsequent sections.

In general, the energy that a LiB cell will release over an upcoming time interval is the integration of its discharging power. This quantity, however, is neither constant nor fixed. Indeed, it is dependent on the discharging C-rate as a result of two main factors. First, the cell's output voltage will decline faster when the discharging current increases, leading to less energy to be released. This phenomenon is known as the rate-capacity effect. Second, the C-rate will greatly influence the cell's temperature. The discharging process and, consequently, the amount of energy that is to be discharged will be subject to the upper temperature limit for safety. RDE's C-rate dependence is too significant to be negligible at high C-rates, demanding a new definition of RDE to fit with discharging over broad current ranges. To proceed, we consider the RDE as the amount of the remaining energy if the cell is discharged at a constant C-rate from the present time until when either the voltage or the temperature limit is reached. With this notion, the RDE is defined as follows:

$$E_{\mathrm{RDE}}(z,t) = \int_{t}^{t+\Delta t_{\mathrm{RDT}}} z c_o V(\tau) d\tau, \qquad (1)$$

where t is the present time, Δt_{RDT} is the remaining discharging time (RDT), z is the future discharge C-rate between t and $t + \Delta t_{\mathrm{RDT}}$, c_o is the current magnitude in ampere when $z = 1$ C, V is the cell's voltage. Note that $t + \Delta t_{\mathrm{RDT}}$ is the time when the cell reaches the cut-off voltage $V_{\min}$ or the maximum allowed temperature $T_{\max}$, whichever earlier, if discharged at the constant current of z C. Fig. 1 illustrates this proposed RDE definition.

The RDE definition in (1) is a departure away from alternative definitions in the literature, e.g., [10], which overlook the effects of
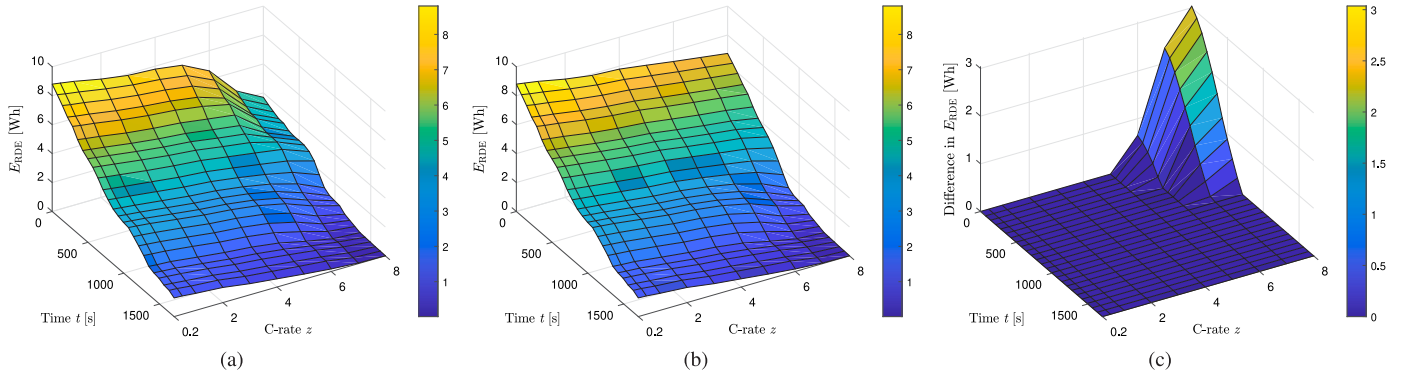
Fig. 2. Variation of the RDE of an NCA cell across different C-rates under a modified US06 discharging profile, with $V_{\min} = 3$ V, $T_{\max} = 50$ °C, and $T_{\text{amb}} = 25$ °C. (a) E_{RDE} subject to the limits of $V_{\min}$ and $T_{\max}$; (b) E_{RDE} subject to only the limit of $V_{\min}$; (c) difference of E_{RDE} between (a) and (b). The results show the C-rate dependence of a cell's RDE and demonstrate the effect of $T_{\max}$ limit for RDE prediction at high discharging C-rates. When only considering $V_{\min}$ limit, the cell's temperature reaches a maximum of 67.5 °C during the prediction of E_{RDE} at $z = 8$ C and $t = 0$ s.

the C-rates. Explicitly included in (1), the C-rate z impacts E_{RDE}, due to its role in changing the evolution of $V(\tau)$ for $t < \tau \leq t + \Delta t_{\text{RDT}}$ and in influencing Δt_{RDT}. Fig. 2(a) illustrates the substantial variation of an NCA cell's E_{RDE} under different z and subject to $V_{\min}$ and $T_{\max}$. It is also interesting to examine how much $T_{\max}$ affects E_{RDE}, so Fig. 2(b) shows E_{RDE} when $T_{\max}$ is disregarded. A significant difference from Fig. 2(a) emerges at high C-rates, which is depicted in Fig. 2(c). This observation underscores the considerable influence of high C-rates on the cell's thermal behavior, while emphasizing the importance of considering $T_{\max}$.

Given the proposed definition, predicting the RDE for a LiB cell involves multiple challenges. First, we need a model that is capable of accurately predicting the cell's voltage and temperature over broad current ranges. Second, even after the model is available, Δt_{RDT} can still be hard to determine as it depends on a mix of the cell's present state, future behavior at designated z, and pre-specified $V_{\min}$ and $T_{\max}$. Finally, online prediction of the RDE is desired, but how to achieve real-time computational efficiency is a question. In the sequel, we will develop a methodical approach to tackle these challenges by utilizing the capabilities of ML. An overview of our study is shown in Fig. 4.

Remark 1. The dependence of a cell's capacity on the discharge C-rate is well-documented in the literature [29]. One empirical method to capture this relationship is the Peukert equation. However, this equation lacks accuracy because it does not account for the cell's dynamics, nor does it incorporate $V_{\min}$ and $T_{\max}$ into the capacity estimation. Meanwhile, the Peukert equation addresses the charge capacity in Ah, but our RDE definition focuses on the energy capacity in Wh. This latter measure is more crucial for practical applications, yet also more challenging to determine due to the voltage dynamics.

3. Hybrid physics-ML modeling for LiBs

This section aims to develop a dynamic model to predict the terminal voltage and temperature of a LiB cell with fast computation and high accuracy when the cell discharging spans broad C-rate ranges. This model will be used to generate high-fidelity synthetic data to train the RDE prediction approach to be proposed in Section 4. We take the approach of integrating physics with ML, following our prior study [24]. For physics-based modeling, we use the nonlinear double capacitor (NDC) model [30] for voltage prediction and a lumped thermal circuit model [31] for temperature prediction.

We begin by introducing the NDC model and the lumped thermal model. The NDC model describes a LiB cell's electric behavior and, different from other ECMs, includes a mechanism to emulate the impact of lithium-ion diffusion on the voltage dynamics. As shown in Fig. 3(a), the model contains two coupled sub-circuits. The first (left) sub-circuit
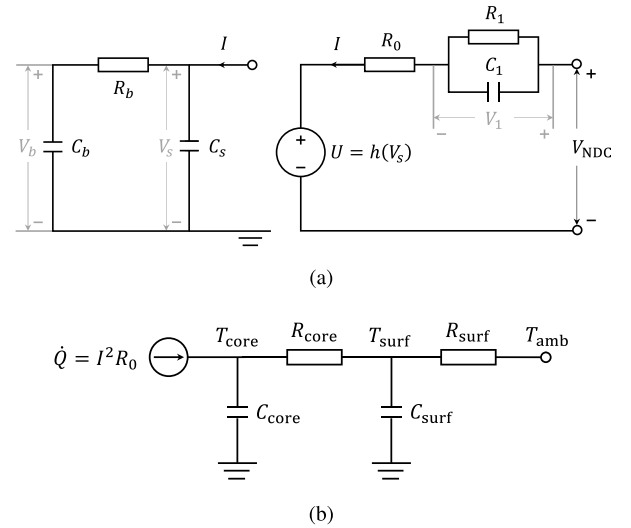
**Fig. 3.** Diagrams of (a) the NDC model and (b) the lumped thermal model.

contains an R–C chain composed of R_b, C_b and C_s. Conceptually, C_b and C_s represent the bulk inner region and surface region of the electrode, respectively; the charge migration between C_b and C_s mimics the lithium-ion diffusion within the electrode. The second (right) sub-circuit contains a voltage source U, a resistor R_0, and an R–C pair R_1-C_1. Here, $U = h(V_s)$ serves as an open-circuit voltage (OCV) source, R_0 corresponds to the ohmic resistance and solid electrolyte interface resistance, and R_1-C_1 accounts for the voltage transients due to charge transfer on the electrode/electrolyte interface. The governing equations of the NDC model are given by

$$\begin{cases} \begin{bmatrix} \dot{V}_b(t) \\ \dot{V}_s(t) \\ \dot{V}_1(t) \end{bmatrix} = A_{\text{NDC}} \begin{bmatrix} V_b(t) \\ V_s(t) \\ V_1(t) \end{bmatrix} + B_{\text{NDC}} I(t), \text{ (a)} \\ V_{\text{NDC}}(t) = h(V_s(t)) + V_1(t) + R_0 I(t), \text{ (b)} \end{cases} \quad (2)$$
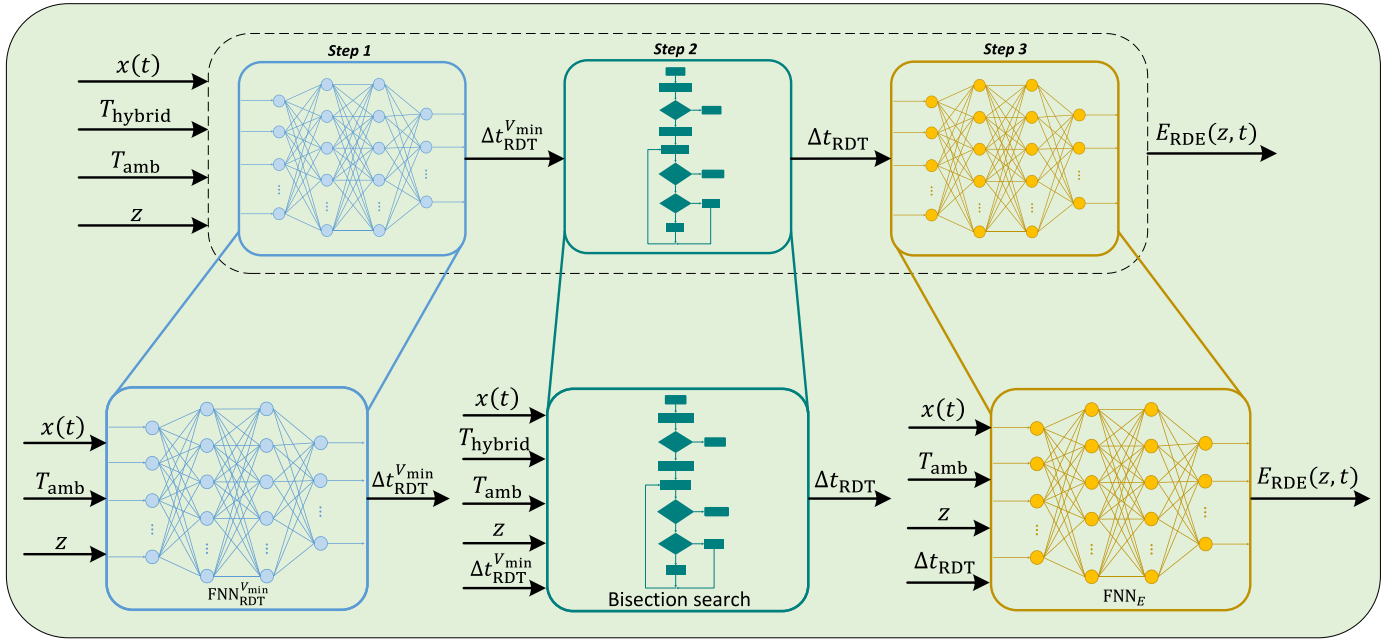
where V_b, V_s and V_1 are the voltages across C_b, C_s and C_1, respectively, and I is the input current ($I < 0$ for discharge, $I > 0$ for charge). Here,

$$A_{\text{NDC}} = \begin{bmatrix} \frac{-1}{C_b R_b} & \frac{1}{C_b R_b} & 0 \\ \frac{1}{C_s R_b} & \frac{-1}{C_s R_b} & 0 \\ 0 & 0 & \frac{-1}{R_1 C_1} \end{bmatrix}, \quad B_{\text{NDC}} = \begin{bmatrix} 0 \\ \frac{1}{C_s} \\ \frac{1}{C_1} \end{bmatrix}.$$

The lumped thermal model, as shown in Fig. 3(b), assumes a cylindrical shape of the cell and concentrates the spatially distributed temperature
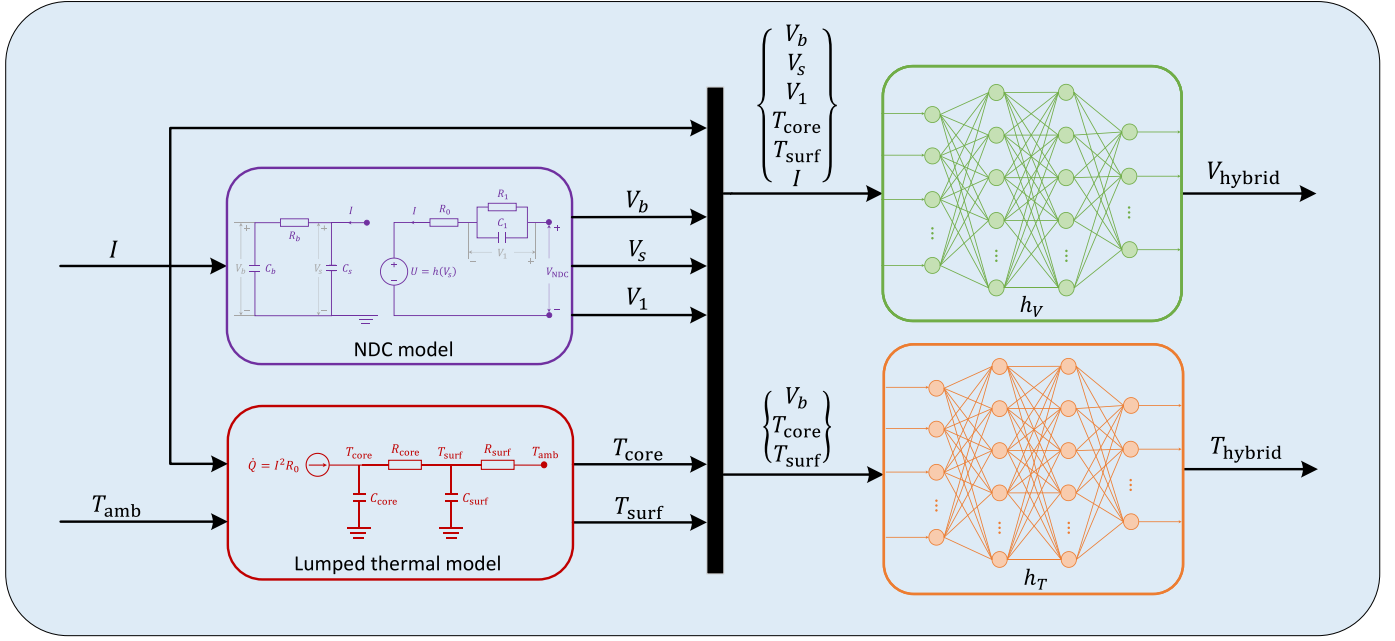
(a)

(b)

Fig. 4. (a) The NDCTNet model, which integrates physics with ML to predict the terminal voltage and temperature of a LiB cell, see Section 3; (b) the pipeline chart of the proposed RDE prediction approach, see Section 4.

radially into two points at the cell's core and the surface, respectively. The model then is governed by

$$\begin{bmatrix} \dot{T}_{core}(t) \\ \dot{T}_{surf}(t) \end{bmatrix} = A_{therm} \begin{bmatrix} T_{core}(t) \\ T_{surf}(t) \end{bmatrix} + B_{therm} \begin{bmatrix} I^2(t) \\ T_{amb} \end{bmatrix}, \tag{3}$$

where

$$A_{therm} = \begin{bmatrix} \frac{-1}{R_{core}C_{core}} & \frac{1}{R_{core}C_{core}} \\ \frac{1}{R_{core}C_{surf}} & \frac{-1}{R_{surf}C_{surf}} + \frac{-1}{R_{core}C_{surf}} \end{bmatrix},$$

$$B_{therm} = \begin{bmatrix} \frac{R_0}{C_{core}} & 0 \\ 0 & \frac{1}{R_{surf}C_{surf}} \end{bmatrix},$$

$T_{core/surf}$ is the temperature at the core/surface of the cell, T_{amb} is the ambient temperature, and $C_{core/surf}$ is the heat capacity at the cell's core/surface. Further, R_{core} is the thermal resistance due to the conduction between the core and surface, and R_{surf} is the thermal resistance due to the convection between the cell's surface and the environment. This model only considers internal heat generation at the core that results from Joule heating.

The above two ECMs have decent accuracy at low to medium C-rates but lack accuracy for high C-rates. To overcome the gap, we couple them with ML models. ML has strong data-driven representation capabilities, and we have shown in our prior study [24] that they can predict the behaviors of a LiB cell with high accuracy if integrated

with physics-based models. Based on the insights in [24], we propose the NDCTNet model in Fig. 4(a), which characteristically connects the above two ECMs with two separate feedforward neural networks (FNNs) in series. The first FNN is responsible for the terminal voltage prediction. It takes V_b, V_s, V_1, T_{core}, T_{surf} and I as the inputs. The second FNN is tasked to predict the surface temperature, and its input includes V_b, T_{core} and T_{surf}. Here, the FNNs are made to use physical state information for prediction. This allows to use simpler FNNs, reduce data dependence in training, and achieve more accurate prediction. It should be noted that the inputs to the FNNs must be selected so that the FNNs can capture physically justifiable mappings [24]. The proposed choice is the best one that we could find after many trials, though there may exist alternatives.

In summary, the NDCTNet model can be written in the following mathematical form:

$$\begin{cases} \dot{x} = f_{phy}(x, I, T_{amb}), & \text{(a)} \\ V_{hybrid} = h_V(x, I), & \text{(b)} \\ T_{hybrid} = h_T(x), & \text{(c)} \end{cases} \tag{4}$$

where $x = [V_b \ V_s \ V_1 \ T_{core} \ T_{surf}]^\top$, (4a) results from (2a) and (3) and is a linear ordinary differential equation, and h_V and h_T represent the two FNNs.

The identification of the NDCTNet model follows a two-step procedure. First, we extract the NDC model and the thermal circuit model from experimental datasets collected at low- to medium-C-rate discharging. The data include current, voltage, and surface temperature, and the parameter estimation is achieved by fitting the models with the data in a least-squares manner [30]. Next, we perform additional discharging tests across low to high C-rates and run the NDC model and the lumped thermal model under the same current profiles. We then train the FNNs, h_V and h_T, using the new datasets. The reader is referred to [24] for more information.

Remark 2. Various physics-based battery models have flourished in the literature, including electrochemical models [32,33] and ECMs [34]. These models provide physical interpretability, but struggle with either computational efficiency or predictive accuracy. Recently, ML has emerged as a powerful tool for data-driven prediction of battery behaviors. While computationally fast and accurate they are, ML models often lack physical consistency while requiring large amounts of training data. However, our previous study [24] shows that integrating physics-based modeling with ML can enable high accuracy, low computation, and reduced dependence on training data. The NDCTNet model extends the work in [24] by incorporating temperature prediction in addition to voltage prediction.

4. Real-time RDE prediction via NNs

In this section, we focus on the problem of real-time RDE prediction for LiBs. Note that, given the LiB model developed in Section 3, a straightforward approach to the RDE prediction is to forward run the NDCTNet model from the present state until V_{min} or T_{max} is reached, as is reported in some existing studies, e.g., [22]. However, this approach requires high computational costs. This is because not only the model execution may take a long time, as the actual discharging can be up to hours, but also the model must be solved for different C-rates from low to high. Therefore, we propose an ML-based approach to enable real-time RDE prediction. This new approach will eliminate the need for repetitive forward model simulation as ML models can give predictions efficiently after being trained. Also, we can harness the capacity of ML to achieve high RDE prediction accuracy given abundant data.

Based on the definition of E_{RDE} in (1), we aim to train an FNN which will output E_{RDE} based on the present state $x(t)$, z and Δt_{RDT}. Here, a key problem is to determine Δt_{RDT}. As the RDT, Δt_{RDT} will depend on whichever of V_{min} and T_{max} comes first in discharging, implying

$$\Delta t_{RDT} = \min\left\{\Delta t_{RDT}^{V_{min}}, \Delta t_{RDT}^{T_{max}}\right\}, \tag{5}$$

where $\Delta t_{RDT}^{V_{min}}$ (resp. $\Delta t_{RDT}^{T_{max}}$) is the time duration that elapses before the cell reaches V_{min} (resp. T_{max}). It should be noted that both $\Delta t_{RDT}^{V_{min}}$ and $\Delta t_{RDT}^{T_{max}}$ are z-dependent. We find out that there exists a mapping from $x(t)$, z and T_{amb} to $\Delta t_{RDT}^{V_{min}}$, which can be captured by an FNN. However, $\Delta t_{RDT}^{T_{max}}$ is much more difficult to compute since the cell constantly has heat exchange with the ambient environment, and the ambient temperature, T_{amb}, can be arbitrary. As it is intractable to train an FNN to predict $\Delta t_{RDT}^{T_{max}}$, we use the bisection method instead to find $\Delta t_{RDT}^{T_{max}}$ if the cell will exceed T_{max} before the elapse of $\Delta t_{RDT}^{V_{min}}$. To sum up, the proposed RDE prediction approach includes the following three steps:

- leverage an FNN to compute $\Delta t_{RDT}^{V_{min}}$ based on $x(t)$, z and T_{amb};
- let $\Delta t_{RDT} = \Delta t_{RDT}^{V_{min}}$ if $\Delta t_{RDT}^{T_{max}} > \Delta t_{RDT}^{V_{min}}$; otherwise, use the bisection search to find out $\Delta t_{RDT}^{T_{max}}$, and let $\Delta t_{RDT} = \Delta t_{RDT}^{T_{max}}$;
- given Δt_{RDT}, use an FNN to predict E_{RDE} based on $x(t)$, z and T_{amb}.

Below we present the details of each step.

4.1. Computation of $\Delta t_{RDT}^{V_{min}}$

The first step aims to use an FNN to predict $\Delta t_{RDT}^{V_{min}}$ based on the triplet $(x(t), z, T_{amb})$. However, one may wonder whether FNNs are able to perform the task. It is known that FNNs are suitable for approximating continuous mappings due to the universal approximation theorem [35], so the question is whether there exists such a mapping from $(x(t), z, T_{amb})$ to a unique $\Delta t_{RDT}^{V_{min}}$. To find the answer, we conduct the following analysis.

We begin with considering (4). Note that (4a) is a linear time-invariant system and thus has a closed-form solution. Letting $x(t)$ be the initial condition, we express the solution $x(t + \Delta t)$ for an arbitrary time interval $\Delta t > 0$ under given z and T_{amb} as

$$x(t + \Delta t) = \phi(x(t), zc_o, T_{amb}; \Delta t),$$

where the exact formula for ϕ is available, see Appendix. Then,

$$V_{hybrid}(t + \Delta t) = h_V \circ \phi(x(t), zc_o, T_{amb}; \Delta t), \tag{6}$$

where $\circ$ denotes the operation of function composition. We further define $h_V^\phi = h_V \circ \phi$ and absorb c_o into it for notational simplicity. Then, $\Delta t_{RDT}^{V_{min}}$ must satisfy

$$h_V^\phi(x(t), z, T_{amb}; \Delta t_{RDT}^{V_{min}}) = V_{min}. \tag{7}$$

The following observations arise out of the equality in (7). First, by selecting a suitable activation function for the NNs, h_V^ϕ is continuously differentiable because both h_V and ϕ are continuously differentiable. Second, for any physically possible $(x(t), z, T_{amb})$, there always exists a unique $\Delta t_{RDT}^{V_{min}}$ in discharging to make (7) hold true. Third, from a physical perspective, it is arguable that an open neighborhood of $(x(t), z, T_{amb})$ would correspond to an open neighborhood of $\Delta t_{RDT}^{V_{min}}$. Finally, when the cell is continuously discharged starting from $x(t)$ and under given z and T_{amb}, its terminal voltage will decline monotonically when the discharging time approaches $\Delta t_{RDT}^{V_{min}}$. This implies

$$\left.\frac{\partial h_V^\phi}{\partial \Delta t}\right|_{\Delta t = \Delta t_{RDT}^{V_{min}}} < 0.$$

Then, by the global implicit function theorem in [36], there is a unique and continuous mapping from $(x(t), z, T_{amb})$ to $\Delta t_{RDT}^{V_{min}}$. With the existence of such a mapping, an FNN can be used to predict $\Delta t_{RDT}^{V_{min}}$ based on $(x(t), z, T_{amb})$, which is denoted as

$$\Delta t_{RDT}^{V_{min}} = \text{FNN}_{RDT}^{V_{min}}(x(t), z, T_{amb}).$$
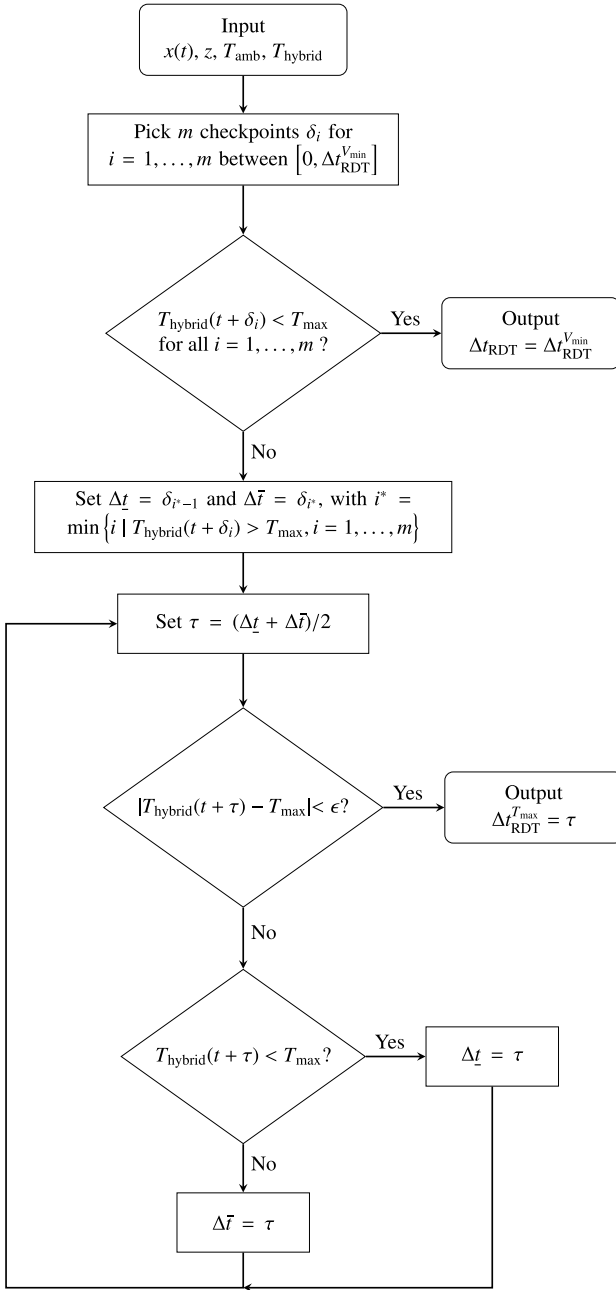
Fig. 5. Bisection search for $\Delta t_{\mathrm{RDT}}^{T_{\max}}$.

4.2. Computation of $\Delta t_{\mathrm{RDT}}^{T_{\max}}$

In predicting the RDE, we must take the cell's future temperature into account to ensure that the prediction lies within the thermal safety bounds. This is particularly vital when the cell runs at high C-rates or under high ambient temperature. We have defined $\Delta t_{\mathrm{RDT}}^{T_{\max}}$ earlier to capture the RDT due to $T_{\max}$. Note that $\Delta t_{\mathrm{RDT}}^{T_{\max}}$ needs to be computed for the RDE prediction only when it is less than $\Delta t_{\mathrm{RDT}}^{V_{\min}}$, as implied by (5). Therefore, it is plausible to expediently determine whether $\Delta t_{\mathrm{RDT}}^{T_{\max}} < \Delta t_{\mathrm{RDT}}^{V_{\min}}$, and in case of not, a fast search for $\Delta t_{\mathrm{RDT}}^{T_{\max}}$ will ensue next.

To check $\Delta t_{\mathrm{RDT}}^{T_{\max}} < \Delta t_{\mathrm{RDT}}^{V_{\min}}$, we pick m checkpoints, δ_i for $i = 1, \ldots, m$, which spread evenly within the interval $\left[0, \Delta t_{\mathrm{RDT}}^{V_{\min}}\right]$. One may choose an appropriate m, depending on the characteristics of the cell's thermal dynamics and the immediate ambient conditions. Then, $T_{\mathrm{hybrid}}(t + \delta_i)$ is

computed for each δ_i via

$$T_{\mathrm{hybrid}}(t + \delta_i) = \underbrace{h_T \circ \phi}_{h_T^\phi} (x(t), z, T_{\mathrm{amb}}; \delta_i).$$

The computation would be efficient, thanks to the closed-form formula of ϕ. We can skip the calculation of $\Delta t_{\mathrm{RDT}}^{T_{\max}}$ if $T_{\mathrm{hybrid}}(t + \delta_i) < T_{\max}$ for all $i = 1, \ldots, m$. Otherwise, we must determine $\Delta t_{\mathrm{RDT}}^{T_{\max}}$, and this is equivalent to finding the root of

$$T_{\mathrm{hybrid}}(t + \delta t) = h_T^\phi(x(t), z, T_{\mathrm{amb}}; \delta t) = T_{\max}, \qquad (8)$$

for which δt is the unknown variable. To achieve this, we apply the bisection method, a popular and efficient root-finding algorithm.

The bisection search is conducted within the interval $[\underline{\Delta t}, \overline{\Delta t}]$. Initially, $\overline{\Delta t} = \delta_{i^*}$ with $i^* = \min\left\{i \mid T_{\mathrm{hybrid}}(t + \delta_i) > T_{\max}, i = 1, \ldots, m\right\}$, and $\underline{\Delta t} = \delta_{i^*-1}$. Assume that there is only one root for (8) within the initial interval. Subsequently, we bisect the interval, evaluate T_{hybrid} at the midpoint, identify the next subinterval to search, and repeat the search procedure. The steps are as follows.

[Step 1] calculate $\tau = (\underline{\Delta t} + \overline{\Delta t})/2$, and evaluate $T_{\mathrm{hybrid}}(t + \tau)$;

[Step 2] let $\Delta t_{\mathrm{RDT}}^{T_{\max}} = \tau$ and stop if $|T_{\mathrm{hybrid}}(t + \tau) - T_{\max}| < \epsilon$, where ϵ is the tolerance; otherwise, go to Step 3.

[Step 3] let $\underline{\Delta t} = \tau$ if $T_{\mathrm{hybrid}}(t + \tau) < T_{\max}$, and let $\overline{\Delta t} = \tau$ if otherwise; go to Step 1.

Fig. 5 shows a flowchart of the procedure. The bisection search can find out $\Delta t_{\mathrm{RDT}}^{T_{\max}}$ fast here. This is because an explicit formula is available for the computation of $T_{\mathrm{hybrid}}(t + \tau)$, and the bisection method converges fast by itself when a unique root exists within the search interval.

4.3. Prediction of E_{RDE}

After identifying Δt_{RDT}, we are now ready to enable the prediction of E_{RDE}. It is beneficial here to consider a more general task — predicting $E(z, t, \Delta t)$, which is the discharging energy released by the cell within the upcoming time interval $(t, t + \Delta t]$ under a constant C-rate z:

$$E(z, t, \Delta t) = \int_t^{t+\Delta t} z c_o V(\tau) d\tau.$$

When $E(z, t, \Delta t)$ is available, we can easily compute E_{RDE} by inserting Δt_{RDT} into it

$$E_{\mathrm{RDE}}(z, t) = E(z, t, \Delta t_{\mathrm{RDT}}). \qquad (9)$$

Given (6), we have

$$E(z, t, \Delta t) = \int_0^{\Delta t} z c_o h_V^\phi(x(t), z, T_{\mathrm{amb}}; \tau) d\tau. \qquad (10)$$

This relation indicates that there exists a continuous mapping from $(x(t), z, T_{\mathrm{amb}}, \Delta t)$ to E. While there is no analytical form of the mapping, we can use an FNN to approximate it. The FNN is denoted as

$$E(z, t, \Delta t) = \mathrm{FNN}_E(x(t), z, T_{\mathrm{amb}}, \Delta t).$$

After the FNN is trained, we can compute E_{RDE} by (9).

Fig. 4(b) presents the pipeline of the proposed RDE prediction approach. To sum up, it is challenging to predict the RDE when the cell shows complex voltage and thermal behaviors under discharging across low to high currents. To overcome this problem, we turn our attention to utilizing the power of ML. We exploit FNNs to capture the sophisticated relationship between the RDE and the many factors that affect it. The approach presents several benefits. First, it is amenable to training. This is because we can train the FNNs on synthetic data generated by running the NDCTNet model in Section 3. This greatly reduces reliance on data collection from experiments, as now only the NDCTNet training requires experimental data. Second, the approach can attain high accuracy when the NDCTNet model is accurate enough to generate good-quality training data in large amounts. Finally, the

Fig. 6. The PEC® SBT4050 battery tester.

Table 1
Specifications of the NCA and LFP cells.

	NCA	LFP
Nominal capacity (Ah)	2.5	2.5
Allowed voltage range (V)	2.5~4.2	2.0~3.6
Max. continuous discharge current (A)	20	50
Operating surface temperature (°C)	−20~75	−30~55

Table 2
Validation results for the two NDCTNet models constructed for the NCA and LFP cells.

LiB type	Current profile	RMSE V_{hybrid}	RMSE T_{hybrid}
NCA	Modified US06 (0~8 C)	12.25 mV	0.27 °C
	Modified SC04 (0~8 C)	13.36 mV	0.56 °C
LFP	Modified US06 (0~15 C)	13.01 mV	0.28 °C
	Modified SC04 (0~15 C)	11.11 mV	0.46 °C

prediction is computationally fast and efficient after the training, as we only need to run the FNNs and, if there is a need, the bisection search procedure.

The proposed ML approach is distinct from existing RDE prediction methods in multiple ways. First, it tackles the challenge of RDE prediction under discharging over broad current ranges, a topic that has not been studied before. Second, to deal with this complex problem, the approach presents a customized ML architecture, which includes and combines different learning modules into a holistic framework. Finally, the design of each module is justified in rationale to ensure its technical soundness, which has been rarely done in previous studies on RDE prediction.

5. Experimental validation

In this study, the experimental validation is performed on two cylindrical LiB cells: a Samsung INR18650-25R cell with an NCA cathode and a graphite anode, and an A123 ANR26650-M1B cell with an LFP cathode and a graphite anode. Table 1 lists their specifications. A PEC® SBT4050 battery tester shown in Fig. 6 was used to charge/discharge the cells and collect experimental data. A thermocouple was attached to each cell's surface to measure its temperature. During the experiments, the cells were placed in a thermal chamber with the ambient temperature set to $T_{amb} = 25$ °C. A host computer with a 2.2 GHz Intel® i7-8750H CPU and 16.0 GB RAM was used to process the collected data and implement the proposed RDE prediction approach.

The validation consists of two stages. In the first stage, we identify and validate the NDCTNet model constructed in Section 3 using experimental data. In the second stage, we run the NDCTNet model in simulations to generate the synthetic data and train the RDE prediction

approach. After the training, we implement the approach and compare its RDE prediction results with the experimental truth.

5.1. Training and validation of the NDCTNet model

We used the following procedure to construct and validate the NDCTNet model for each of the two cells.

As the first step, we identified the NDC model and the lumped thermal model for each cell based on the methods in [30,31]. Then, we moved on to train the FNNs of each NDCTNet model.

- The NDC model was identified using the parameter identification 1.0 approach in [30]. The lumped thermal model had been identified for the Samsung NCA cell in [37] and for the A123 LFP cell in [31]. We made some fine tuning of the parameters to make them fit better with our data.
- We used the same FNN architecture for h_V and h_T for both cells. The FNN has two hidden layers with 48 neurons in each hidden layer. The softplus function is used as the activation function of the hidden layers, and the output layer employs the linear activation function. The FNNs are configured and trained using Keras, a Python-based deep learning library. The input data normalization was applied to the FNNs.
- For the NCA cell, we collected the training datasets via constant-current discharging at 0.5/1/3/5/8 C and variable-current discharging based on the modified HWFET/UDDS/WLTC/LA92 profiles (scaled to 0~8 C) [38]. The datasets include 22,770 datapoints in total.
- For the LFP cell, the training datasets were generated by applying constant-current discharging at 0.5/1/2/4/6/8/10/12/15 C and variable-current discharging based on the modified HWFET/UDDS/WLTC/LA92 profiles (scaled to 0~15 C). The datasets contain 23,341 datapoints in total.
- We use the root-mean-square error (RMSE) as a metric to evaluate the NDCTNet model's prediction performance:

$$\text{RMSE} = \sqrt{\frac{1}{N}\sum_{i=1}^{N}\left(X_{\text{true},i} - X_{\text{NDCTNet},i}\right)^2},$$

where $X_{\text{true},i}$ is the true voltage/temperature at the ith datapoint, $X_{\text{NDCTNet},i}$ is the predicted voltage/temperature, and N is the total number of datapoints.

Further, we collected extra datasets based on the modified US06/SC04 profiles, scaled to 0~8 C for the NCA cell and 0~15 C for the LFP cell, to test the NDCTNet model after training. Figs. 7–8 present the validation results, which show excellent fitting performance. Table 2 offers a quantitative evaluation based on the RMSE, indicating that the NDCTNet model exhibits high accuracy over broad current ranges for each cell.

5.2. Validation of the RDE prediction approach

Based on the identified NDCTNet model, we continue to validate the proposed RDE prediction approach. First, we simulate the discharging processes using the NDCTNet model and leverage the obtained synthetic data to train the FNNs used in the approach. After the training, we validate the approach by comparing the prediction with the experimental results based on additional discharging experiments.

In the training stage, the setting is as follows.

- The cut-off limits in the RDE prediction are: $V_{\min} = 3$ V and $T_{\max} = 50$ °C for the NCA cell, and $V_{\min} = 2.7$ V and $T_{\max} = 45$ °C for the LFP cell. They are chosen based on manufacturer specifications and related literature [39].
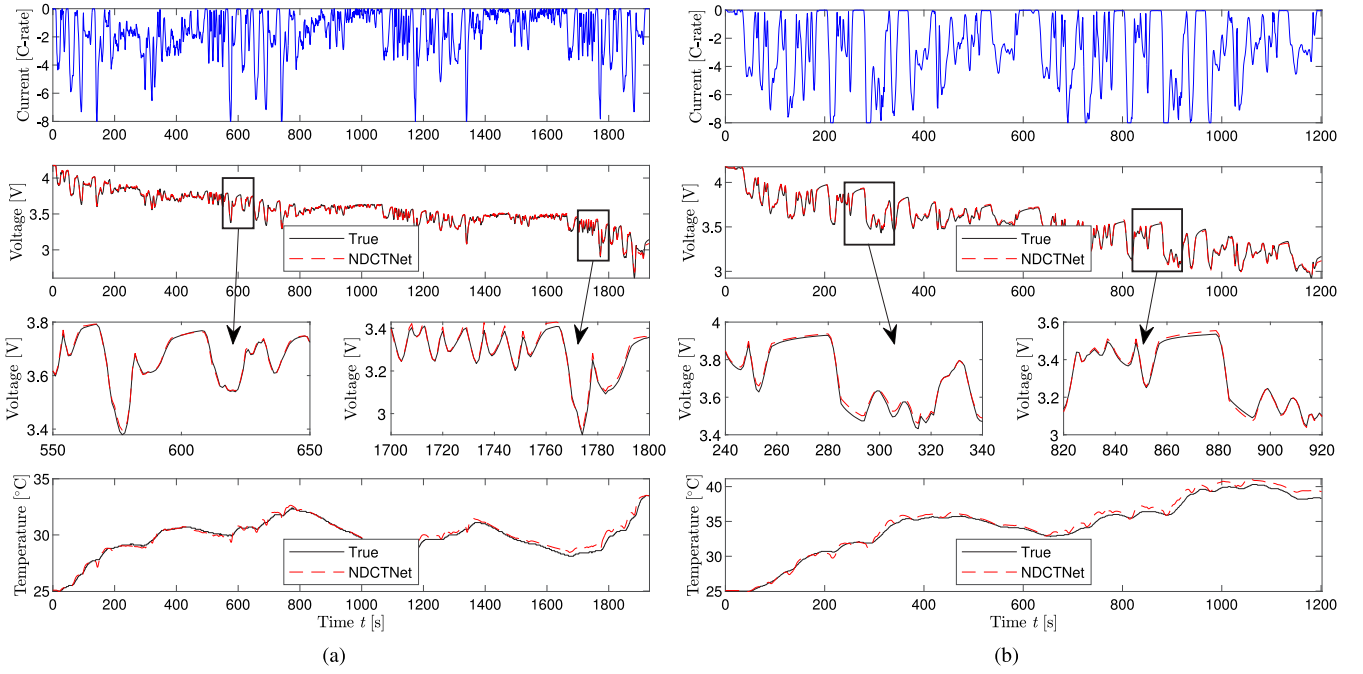
Fig. 7. Validation of the NDCTNet model for the NCA cell based on (a) the modified US06 (0∼8 C) and (b) the modified SC04 (0∼8 C) profiles.
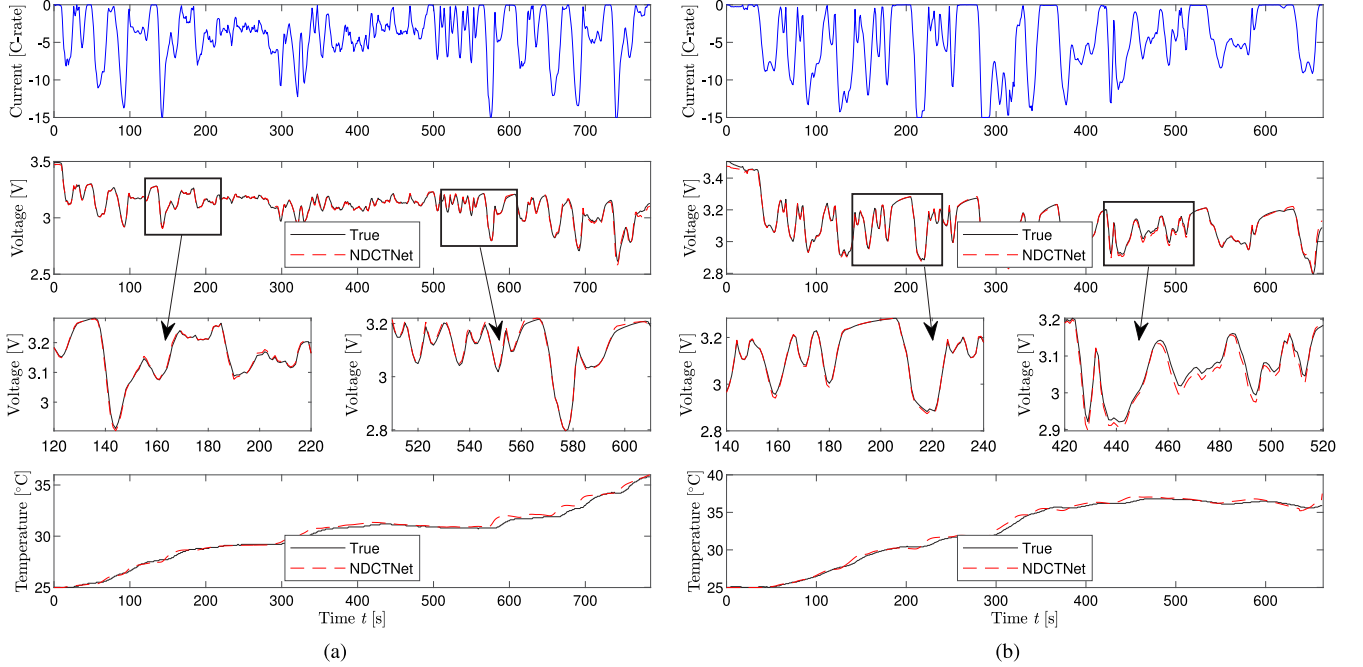

Fig. 8. Validation of the NDCTNet model for the LFP cell based on (a) the modified US06 (0∼15 C) and (b) the modified SC04 (0∼15 C) profiles.

- All the FNNs used in the RDE prediction for both cells have the same architecture of two hidden layers with each having 48 neurons. They are also configured and trained using Keras as in Section 5.1.
- We construct synthetic training datasets via simulation based on the NDCTNet models. For the NCA cell, the discharging simulation is based on the modified variable-current HWFET/UDDS/ WLTC/LA92 profiles (scaled to 0∼8 C). In each discharging case,

we branch out to run episodic simulations at every time instant t, which discharge the cell fully to V_{min} at different constant C-rates ranging between 0.2∼8 C. With the generated data, we determine $\Delta t_{RDT}^{V_{min}}$ that corresponds to the cell's state $x(t)$ and C-rate z. Meanwhile, we compute $E(z, t, \Delta t)$ for each $\Delta t \in \left[0, \Delta t_{RDT}^{V_{min}}\right]$. These data are utilized to train the FNNs in the RDE prediction approach, with 160,867 datapoints for the $FNN_{RDT}^{V_{min}}$ network and
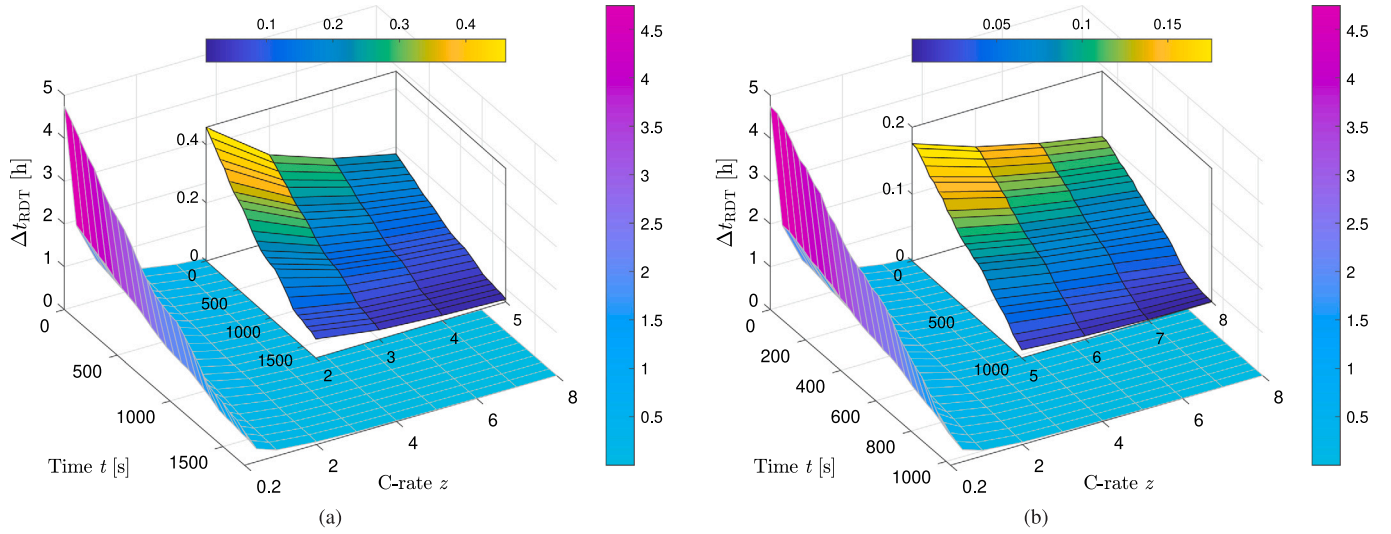
Fig. 9. RDT prediction results for the NCA cell under (a) the modified US06 (0~8 C) and (b) the modified SC04 (0~8 C) testing profiles at $T_{amb} = 25$ °C. The inset plots highlight the RDT at high C-rate loads.
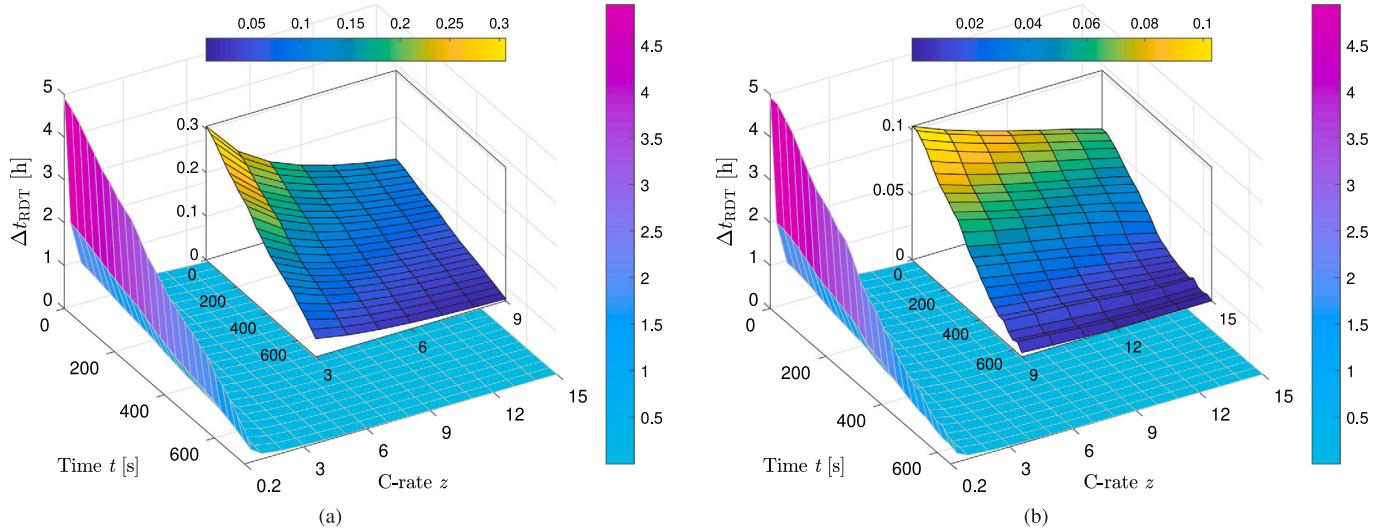
Fig. 10. RDT prediction results for the LFP cell under (a) the modified US06 (0~15 C) and (b) the modified SC04 (0~15 C) testing profiles at $T_{amb} = 25$ °C. The inset plots highlight the RDT at high C-rate loads.

33,068,654 datapoints for the FNN_E network. The same is done for the LFP cell, with the current range in the simulation adjusted to be 0.2~15 C. The training datasets contain 263,195 datapoints for $\text{FNN}_{\text{RDT}}^{V_{\min}}$ and 36,439,162 datapoints for FNN_E.

- We introduce a percentage relative error to quantify the prediction accuracy:

$$\text{Relative error} = \left| \frac{Y_{\text{true}} - Y_{\text{pred}}}{Y_{\text{true}}} \right| \times 100\%,$$

where Y is Δt_{RDT} or E_{RDE}.

Following the training, we apply the approach to the two cells discharged with the modified US06/SC04 profiles for the purpose of validation. For each time instant t during the discharge, we predict the RDT for different C-rate loads between $z = 0.2$~8 C for the NCA cell and $z = 0.2$~15 C for the LFP cell. Figs. 9–10 show the predicted RDT as part of the RDE prediction, in which the inset plots highlight the RDT at high C-rates. Figs. 11–12 illustrate the RDE prediction results.

We observe that both the RDT and RDE decrease as C-rate increases for both cells due to the rate-capacity effect. Moreover, the predicted RDE drops sharply at very high C-rates ($z = 6$~8 C for the NCA cell and $z = 10$~15 C for the LFP cell). This is because the preset $T_{\max}$ limit is triggered, which further limits E_{RDE}.

We further perform experiments to assess the RDE prediction accuracy for each cell. In each experiment, we discharge the cell using a variable-current profile for some time t and then switch to constant-current discharging at a specified C-rate z so as to determine the actual E_{RDE}. For each cell, both the modified US06/SC04 profiles are used, and for each profile, four different (t, z) pairs are considered. This thus involves experiments for 16 cases in total, as are shown in Figs. 11–12. Table 3 presents a quantitative comparison for all these cases. It is seen that the relative error in the RDE prediction comes less than 3% in general. Besides, when $T_{\max}$ is triggered, E_{RDE} becomes less and more difficult to be predicted. Table 3 shows the cases when this happens, in all of which accurate prediction is still observed.
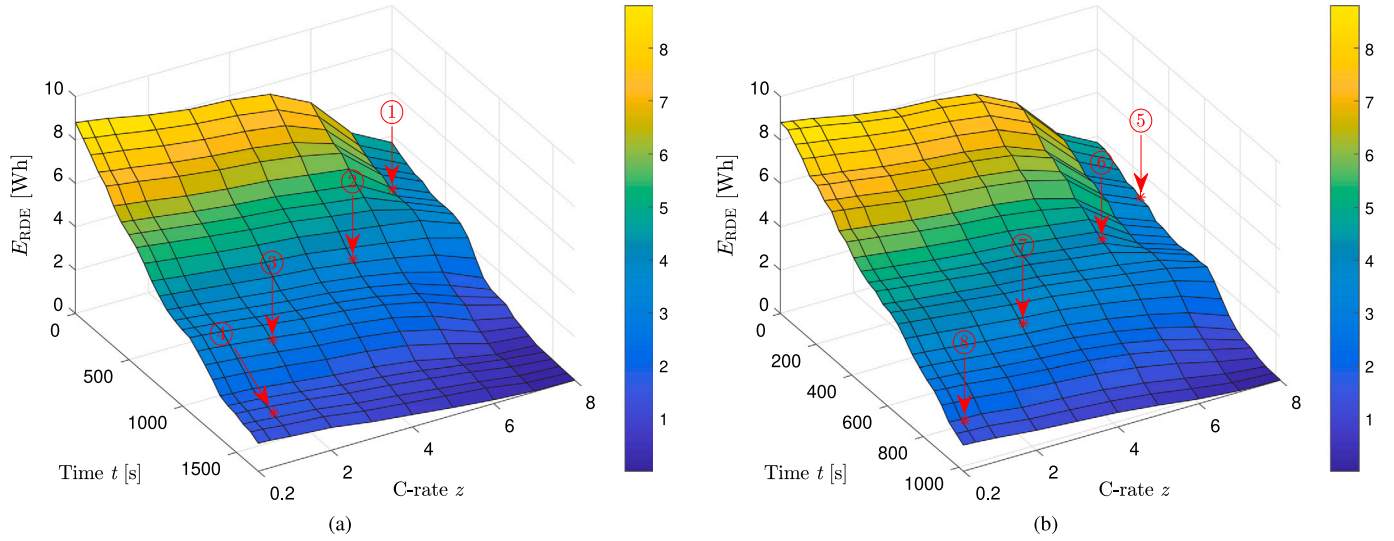
Fig. 11. RDE prediction results for the NCA cell under (a) the modified US06 (0∼8 C) and (b) the modified SC04 (0∼8 C) testing profiles at $T_{\text{amb}} = 25$ °C. "$*$" denotes the experimental validation datapoint at ① $t = 389$ s, $z = 7$, ② $t = 775$ s, $z = 5$, ③ $t = 1161$ s, $z = 2$, ④ $t = 1547$ s, $z = 1$, ⑤ $t = 243$ s, $z = 8$, ⑥ $t = 483$ s, $z = 6$, ⑦ $t = 723$ s, $z = 3$, ⑧ $t = 963$ s, $z = 0.5$.
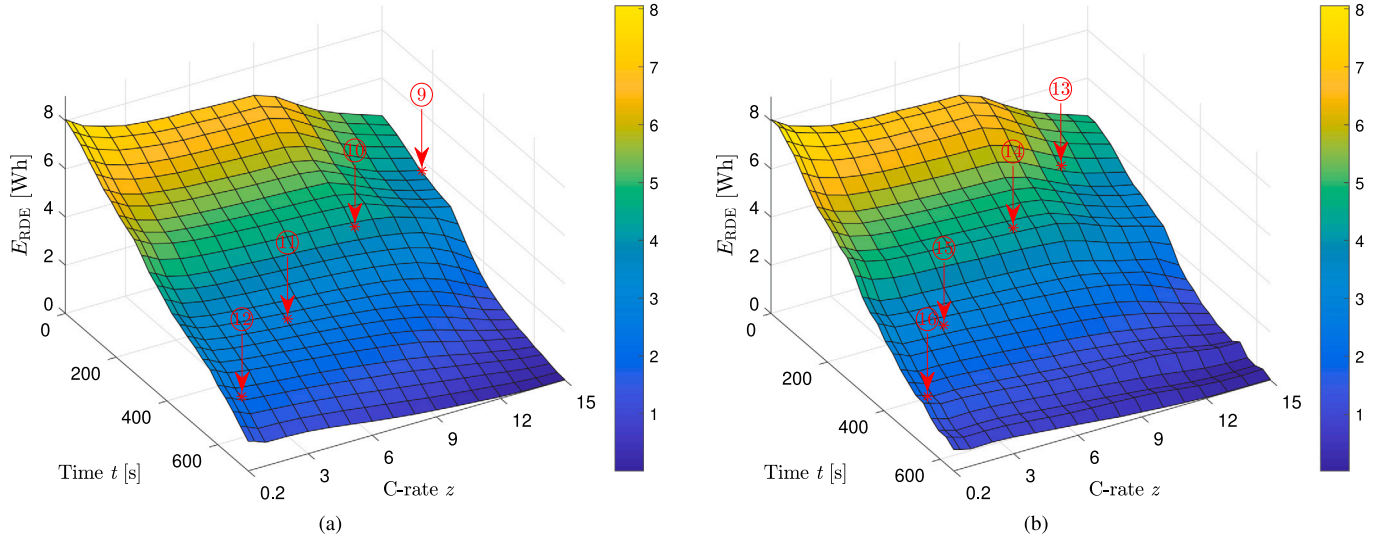
Fig. 12. RDE prediction results for the LFP cell under (a) the modified US06 (0∼15 C) and (b) the modified SC04 (0∼15 C) testing profiles at $T_{\text{amb}} = 25$ °C. "$*$" denotes the experimental validation datapoint at ⑨ $t = 159$ s, $z = 15$, ⑩ $t = 315$ s, $z = 10$, ⑪ $t = 471$ s, $z = 5$, ⑫ $t = 627$ s, $z = 1$, ⑬ $t = 135$ s, $z = 12$, ⑭ $t = 267$ s, $z = 8$, ⑮ $t = 399$ s, $z = 3$, ⑯ $t = 531$ s, $z = 0.5$.

Table 4 compares the computational time of the proposed ML approach with the model forward simulation. Each prediction runs the two methods at all $z = 0.2/0.5/1/2/3/4/5/6/7/8$ C for the NCA cell and all $z = 0.2/0.5/1/2/3/4/5/6/7/8/9/10/11/12/13/14/15$ C for the LFP cell to obtain the RDE corresponding to each specified C-rate. The model forward simulation calculates the RDE by running the NDCTNet model until the cut-off limit is reached. Our ML approach needs only 0.3∼0.4 s for prediction at each time. By contrast, the model forward simulation needs an average time of about 25∼50 s, while demanding a much larger actual time at the beginning of a discharging process.

We further compare our results with a traditional RDE defined as in [10]:

$$E_{\text{RDE}}^{\text{Trad}} = Q_a \int_{\text{SoC}=0}^{\text{SoC}(t)} U_{\text{OCV}}(\text{SoC}) d\,\text{SoC},$$

where Q_a and U_{OCV} are the cell's charge capacity in Ah and OCV, respectively. As shown in Table 3, the prediction of $E_{\text{RDE}}^{\text{Trad}}$ at low C-rates shows a decent accuracy relative to the truth. However, its accuracy

declines greatly as the C-rate increases and becomes almost trivial at very high C-rates. This is because $E_{\text{RDE}}^{\text{Trad}}$, by definition, fails to capture the effects of high C-rates on RDE.

6. Discussion

We provide the following remarks based on the results in Sections 2–5.

- Predictive accuracy. The proposed ML-based RDE prediction approach demonstrates a high accuracy in experimental validation. This is due to two main reasons. First, the proposed ML architecture, which includes multiple learning modules, is well-founded on technical rationale. Second, we generate large amounts of synthetic but high-fidelity data using the NDCTNet model. This makes it possible to push the training accuracy to the best possible extent for the proposed approach.

Table 3

RDE prediction results of the 16 experimental validation datapoints. The preset T_{max} limit is triggered at ① ⑤ ⑨ ⑬.

	LiB type	Current profile	Time instant t [s]	C-rate z	True Δt_{RDT} [s]	Predicted Δt_{RDT} [s] (proposed method)	Relative Δt_{RDT} error (proposed method)	True E_{RDE} [Wh]	Predicted E_{RDE}^{Trad} [Wh] (traditional method)	Relative E_{RDE} error (traditional method)	Predicted E_{RDE} [Wh] (proposed method)	Relative E_{RDE} error (proposed method)
①	NCA	Modified US06 (0~8 C)	389	7	221	231	4.52%	3.64	6.27	72.25%	3.56	2.20%
②			775	5	279	279	0%	3.14	4.14	31.85%	3.11	0.96%
③			1161	2	569	574	0.88%	2.66	3.01	13.16%	2.62	1.50%
④			1547	1	601	639	6.32%	1.47	1.58	7.48%	1.43	2.72%
⑤		Modified SC04 (0~8 C)	243	8	148	154	4.05%	2.81	6.98	148.40%	2.73	2.85%
⑥			483	6	267	276	3.37%	3.69	4.97	34.69%	3.58	2.98%
⑦			723	3	435	445	2.30%	3.09	3.63	17.48%	2.99	3.24%
⑧			963	0.5	1343	1396	3.95%	1.63	1.66	1.84%	1.58	3.07%
⑨	LFP	Modified US06 (0~15 C)	159	15	126	120	4.76%	3.50	6.42	83.43%	3.59	2.57%
⑩			315	10	192	195	1.56%	3.87	4.99	28.94%	3.84	0.78%
⑪			471	5	269	263	2.23%	2.72	3.47	27.57%	2.79	2.57%
⑫			627	1	932	894	4.08%	1.92	2.22	15.63%	1.96	2.08%
⑬		Modified SC04 (0~15 C)	135	12	188	181	3.72%	4.33	6.50	50.12%	4.39	1.39%
⑭			267	8	253	253	0%	4.11	5.04	22.63%	4.15	0.97%
⑮			399	3	426	412	3.29%	2.63	3.02	14.83%	2.70	2.66%
⑯			531	0.5	1601	1548	3.31%	1.68	1.77	5.36%	1.72	2.38%

Table 4

Comparison of the computational speed of the RDE prediction methods for the NCA and LFP cell.

Method	Average RDE computation time	
	NCA ($z = 0.2$~8 C)	LFP ($z = 0.2$~15 C)
Model forward simulation	25 s	50 s
Proposed ML approach	0.3 s	0.4 s

- Computational efficiency. The proposed approach can update the RDE with high computational speed, by leveraging ML to predict the RDE directly using the cell's present state. Compared to it, existing RDE methods have to run a LiB model forward from the present state until the cutoff limit is reached, causing heavy and even prohibitive computation.
- Prospective applications. The proposed approach uniquely enables RDE prediction across a wide range of C-rates, making it particularly suitable for high-power LiB applications. One notable example is electric vertical take-off and landing (eVTOL) aircraft, which require discharging at up to 5 C during the takeoff and landing phases, and around 1.5 C during the cruise phase [40]. To our knowledge, no existing methods can accurately predict RDE for eVTOL applications. Furthermore, when applied to lithium-ion battery systems operating at low to medium currents, the proposed approach will hold a promise to improve both the accuracy and computational speed of RDE predictions.
- Potential extensions. The proposed work offers several avenues for further research. While we have validated our approach on NCA and LFP cells, it would be valuable to apply it to other types of LiBs, such as NMC and LCO. Determining the optimal FNN architectures within our approach remains an intriguing question. We have empirically adjusted the architectures in the study to achieve the best performance, but an automated architecture search could be beneficial. Moreover, our approach using FNNs does not quantify uncertainty, though uncertainty quantification could be important for assessing the confidence levels associated with the RDE prediction. To address this, we could explore the use of probabilistic ML techniques, such as Bayesian neural networks [41].

7. Conclusion

RDE prediction plays an important role in managing the operation of LiBs for high safety and performance. In pursuit of this topic, we consider a new and open question: how to predict the RDE of a LiB cell if the discharging currents span from low to high C-rates? The question has emerged in some applications like electric aircraft but is non-trivial to deal with. This is because high currents will significantly impact the cell's electro-thermal dynamics to make the RDE more difficult to identify. To address the question, we define the RDE as a C-rate-dependent quantity. With the new definition, we develop an ML approach that uses FNNs to grasp the mapping from the cell's present state to the RDE. The approach determines the cell's RDT due to voltage and temperature limits and then uses it along with the cell's state to find out the RDE. To enable the training of the approach, we also develop a hybrid physics-ML model to capture the cell's electro-thermal dynamics. The experimental validation on NCA and LFP cells shows the high prediction accuracy achieved by the proposed approach. Further, the approach is tractable for training and computationally efficient to run. It can find prospective use in different applications ranging from electric cars, heavy-duty vehicles, and aircraft to grid-scale energy storage.

CRediT authorship contribution statement

Hao Tu: Writing – original draft, Visualization, Validation, Methodology, Data curation, Conceptualization. **Manashita Borah:** Writing – review & editing, Investigation. **Scott Moura:** Writing – review & editing, Investigation. **Yebin Wang:** Writing – review & editing, Investigation. **Huazhen Fang:** Writing – review & editing, Supervision, Resources, Methodology, Investigation, Funding acquisition, Formal analysis, Conceptualization.

Declaration of competing interest

The authors declare the following financial interests/personal relationships which may be considered as potential competing interests: Huazhen Fang reports financial support was provided by the U.S. National Science Foundation and by the U.S. Department of Energy. If there are other authors, they declare that they have no known competing financial interests or personal relationships that could have appeared to influence the work reported in this paper.

Data availability

Data will be made available on request.

Appendix

We derive the explicit formulas for ϕ under constant z and T_{amb}.

Letting $x(t)$ be the initial condition, and considering that x is decomposed into $x_1 = \begin{bmatrix} V_b & V_s & V_1 \end{bmatrix}^\top$ and $x_2 = \begin{bmatrix} T_{core} & T_{surf} \end{bmatrix}^\top$. Based on (2a), the solution of x_1 is given by

$$x_1(t + \Delta t) = e^{A_1 \Delta t} x_1(t) + \int_t^{t+\Delta t} e^{A_1(t+\Delta t - \tau)} B_1 I(\tau) d\tau,$$

which, when $I = zc_o$, becomes

$$x_1(t + \Delta t) = e^{A_1 \Delta t} x_1(t) + \int_t^{t+\Delta t} e^{A_1(t+\Delta t - \tau)} d\tau \cdot B_1 zc_o. \tag{A.1}$$

It can be easily proven that A_1 has three distinct eigenvalues λ_i for $i = 1, 2, 3$. By the Cayley–Hamilton theorem, we have

$$e^{A_1 \Delta t} = [\Psi_1^{-1} \psi_1(\Delta t)] \oplus A_1, \tag{A.2}$$

where

$$\Psi_1 = \begin{bmatrix} 1 & \lambda_1 & \lambda_1^2 \\ 1 & \lambda_2 & \lambda_2^2 \\ 1 & \lambda_3 & \lambda_3^2 \end{bmatrix}, \quad \psi_1(\Delta t) = \begin{bmatrix} e^{\lambda_1 \Delta t} & e^{\lambda_2 \Delta t} & e^{\lambda_3 \Delta t} \end{bmatrix}^\top,$$

and the operator $\oplus$ denotes

$$a \oplus A = \sum_{i=1}^{n} a_i A^{i-1},$$

for $a \in \mathbb{R}^{n \times 1}$ and $A \in \mathbb{R}^{n \times n}$. Given (A.2), the integral in (A.1) can be expressed as

$$\begin{aligned} \int_t^{t+\Delta t} e^{A_1(t+\Delta t - \tau)} d\tau &= \int_t^{t+\Delta t} [\Psi_1^{-1} \psi_1(t + \Delta t - \tau)] \oplus A_1 d\tau \\ &= [\Psi_1^{-1} \int_t^{t+\Delta t} \psi_1(t + \Delta t - \tau) d\tau] \oplus A_1 \\ &= [\Psi_1^{-1} \int_0^{\Delta t} \psi_1(\zeta) d\zeta] \oplus A_1 \\ &= [\Psi_1^{-1}(\bar{\psi}_1(\Delta t) - \bar{\psi}_1(0))] \oplus A_1, \end{aligned} \tag{A.3}$$

where $\bar{\psi}_1(\alpha) = \begin{bmatrix} e^{\lambda_1 \alpha}/\lambda_1 & e^{\lambda_2 \alpha}/\lambda_2 & e^{\lambda_3 \alpha}/\lambda_3 \end{bmatrix}^\top$. Inserting (A.2) and (A.3) into (A.1), we have

$$\begin{aligned} x_1(t + \Delta t) = {} & [\Psi_1^{-1} \psi_1(\Delta t)] \oplus A_1 \cdot x_1(t) \\ & + [\Psi_1^{-1}(\bar{\psi}_1(\Delta t) - \bar{\psi}_1(0))] \oplus A_1 \cdot B_1 zc_o. \end{aligned}$$

Similarly, we can obtain

$$\begin{aligned} x_2(t + \Delta t) = {} & [\Psi_2^{-1} \psi_2(\Delta t)] \oplus A_2 \cdot x_2(t) \\ & + [\Psi_2^{-1}(\bar{\psi}_2(\Delta t) - \bar{\psi}_2(0))] \oplus A_2 \cdot B_2 u. \end{aligned}$$

where $u = \begin{bmatrix} (zc_o)^2 & T_{amb} \end{bmatrix}^\top$,

$$\Psi_2 = \begin{bmatrix} 1 & \lambda_4 \\ 1 & \lambda_5 \end{bmatrix}, \quad \psi_2(\Delta t) = \begin{bmatrix} e^{\lambda_4 \Delta t} & e^{\lambda_5 \Delta t} \end{bmatrix}^\top,$$

and $\bar{\psi}_2(\alpha) = \begin{bmatrix} e^{\lambda_4 \alpha}/\lambda_4 & e^{\lambda_5 \alpha}/\lambda_5 \end{bmatrix}^\top$. Here, λ_i for $i = 4, 5$ are the two distinct eigenvalues of A_2.

References

[1] Wang Y, Fang H, Zhou L, Wada T. Revisiting the state-of-charge estimation for lithium-ion batteries: A methodical investigation of the extended Kalman filter approach. IEEE Control Syst Mag 2017;37(4):73–96.

[2] Moura SJ, Argomedo FB, Klein R, Mirtabatabaei A, Krstic M. Battery state estimation for a single particle model with electrolyte dynamics. IEEE Trans Control Syst Technol 2017;25(2):453–68.

[3] Bartlett A, Marcicki J, Onori S, Rizzoni G, Yang XG, Miller T. Electrochemical model-based state of charge and capacity estimation for a composite electrode lithium-ion battery. IEEE Trans Control Syst Technol 2016;24(2):384–99.

[4] Lin X, Stefanopoulou AG, Li Y, Anderson RD. State of charge imbalance estimation for battery strings under reduced voltage sensing. IEEE Trans Control Syst Technol 2015;23(3):1052–62.

[5] Hu L, Hu X, Che Y, Feng F, Lin X, Zhang Z. Reliable state of charge estimation of battery packs using fuzzy adaptive federated filtering. Appl Energy 2020;262:114569.

[6] Zhao S, Duncan SR, Howey DA. Observability analysis and state estimation of lithium-ion batteries in the presence of sensor biases. IEEE Trans Control Syst Technol 2017;25(1):326–33.

[7] Rahimi-Eichi H, Baronti F, Chow M-Y. Online adaptive parameter identification and state-of-charge coestimation for lithium-polymer battery cells. IEEE Trans Ind Electron 2014;61(4):2053–61.

[8] Fang H, Wang Y, Sahinoglu Z, Wada T, Hara S. State of charge estimation for lithium-ion batteries: An adaptive approach. Control Eng Pract 2014;25:45–54.

[9] Mamadou K, Delaille A, Lemaire-Potteau E, Bultel Y. The state-of-energy: A new criterion for the energetic performances evaluation of electrochemical storage devices. ECS Trans 2010;25(35):105.

[10] Quade KL, Jöst D, Sauer DU, Li W. Understanding the energy potential of lithium-ion batteries: Definition and estimation of the state of energy. Batter Supercaps 2023;6(8):e202300152.

[11] Wang Y, Zhang C, Chen Z. An adaptive remaining energy prediction approach for lithium-ion batteries in electric vehicles. J Power Sources 2016;305:80–8.

[12] Zheng L, Zhu J, Wang G, He T, Wei Y. Novel methods for estimating lithium-ion battery state of energy and maximum available energy. Appl Energy 2016;178:1–8.

[13] Zhang X, Wang Y, Wu J, Chen Z. A novel method for lithium-ion battery state of energy and state of power estimation based on multi-time-scale filter. Appl Energy 2018;216:442–51.

[14] Ma L, Hu C, Cheng F. State of charge and state of energy estimation for lithium-ion batteries based on a long short-term memory neural network. J Energy Storage 2021;37:102440.

[15] Dong G, Zhang X, Zhang C, Chen Z. A method for state of energy estimation of lithium-ion batteries based on neural network model. Energy 2015;90:879–88.

[16] Zhang W, Shi W, Ma Z. Adaptive unscented Kalman filter based state of energy and power capability estimation approach for lithium-ion battery. J Power Sources 2015;289:50–62.

[17] He H, Zhang Y, Xiong R, Wang C. A novel Gaussian model based battery state estimation approach: State-of-energy. Appl Energy 2015;151:41–8.

[18] Xiong R, Zhang Y, He H, Zhou X, Pecht MG. A double-scale, particle-filtering, energy state prediction algorithm for lithium-ion batteries. IEEE Trans Ind Electron 2018;65(2):1526–38.

[19] Wang Y, Chen Z. A framework for state-of-charge and remaining discharge time prediction using unscented particle filter. Appl Energy 2020;260:114324.

[20] Quiñones F, Milocco R, Real S. Remaining discharge-time prediction for batteries using the Lambert function. J Power Sources 2018;400:256–63.

[21] Pola DA, Navarrete HF, Orchard ME, Rabié RS, Cerda MA, Olivares BE, Silva JF, Espinoza PA, Pérez A. Particle-filtering-based discharge time prognosis for lithium-ion batteries with a statistical characterization of use profiles. IEEE Trans Reliab 2015;64(2):710–20.

[22] Niri MF, Bui TM, Dinh TQ, Hosseinzadeh E, Yu TF, Marco J. Remaining energy estimation for lithium-ion batteries via Gaussian mixture and Markov models for future load prediction. J Energy Storage 2020;28:101271.

[23] Yang X-G, Liu T, Ge S, Rountree E, Wang C-Y. Challenges and key requirements of batteries for electric vertical takeoff and landing aircraft. Joule 2021;5(7):1644–59.

[24] Tu H, Moura S, Wang Y, Fang H. Integrating physics-based modeling with machine learning for lithium-ion batteries. Appl Energy 2023;329:120289.

[25] Nozarijouybari Z, Fathy HK. Machine learning for battery systems applications: Progress, challenges, and opportunities. J Power Sources 2024;601:234272.

[26] Aykol M, Gopal CB, Anapolsky A, Herring PK, van Vlijmen B, Berliner MD, Bazant MZ, Braatz RD, Chueh WC, Storey BD. Perspective — Combining physics and machine learning to predict battery lifetime. J Electrochem Soc 2021;168(3):030525.

[27] Guo W, Sun Z, Vilsen SB, Meng J, Stroe DI. Review of "grey box" lifetime modeling for lithium-ion battery: Combining physics and data-driven methods. J Energy Storage 2022;56:105992.

[28] Thelen A, Huan X, Paulson N, Onori S, Hu Z, Hu C. Probabilistic machine learning for battery health diagnostics and prognostics — review and perspectives. Npj Mater Sustain 2024;2:14.

[29] Doerffel D, Sharkh SA. A critical review of using the Peukert equation for determining the remaining capacity of lead-acid and lithium-ion batteries. J Power Sources 2006;155(2):395–400.

[30] Tian N, Fang H, Chen J, Wang Y. Nonlinear double-capacitor model for rechargeable batteries: Modeling, identification, and validation. IEEE Trans Control Syst Technol 2021;29(1):370–84.

[31] Lin X, Perez HE, Mohan S, Siegel JB, Stefanopoulou AG, Ding Y, Castanier MP. A lumped-parameter electro-thermal model for cylindrical batteries. J Power Sources 2014;257:1–11.

[32] Krewer U, Röder F, Harinath E, Braatz RD, Bedürftig B, Findeisen R. Review— dynamic models of Li-ion batteries for diagnosis and operation: A review and perspective. J Electrochem Soc 2018;165(16):A3656–73.

[33] Chaturvedi NA, Klein R, Christensen J, Ahmed J, Kojic A. Algorithms for advanced battery-management systems. IEEE Control Syst Mag 2010;30(3):49–68.

[34] Hu X, Li S, Peng H. A comparative study of equivalent circuit models for li-ion batteries. J Power Sources 2012;198:359–67.

[35] Hornik K, Stinchcombe M, White H. Multilayer feedforward networks are universal approximators. Neural Netw 1989;2(5):359–66.

[36] Sandberg I. Global implicit function theorems. IEEE Trans Circuits Syst 1981;28(2):145–9.

[37] Biju N, Fang H. BattX: An equivalent circuit model for lithium-ion batteries over broad current ranges. Appl Energy 2023;339:120905.

[38] Vehicle and fuel emission testing. Technical report, Environmental Protection Agency.

[39] Bandhauer TM, Garimella S, Fuller TF. A critical review of thermal issues in lithium-ion batteries. J Electrochem Soc 2011;158(3):R1.

[40] Bills A, Sripad S, Fredericks L, Guttenberg M, Charles D, Frank E, Viswanathan V. A battery dataset for electric vertical takeoff and landing aircraft. Sci Data 2023;10:344.

[41] Ghahramani Z. Probabilistic machine learning and artificial intelligence. Nature 2015;521:452–9.